Strong spin-orbit coupling and Dirac nodal lines in the three-dimensional electronic structure of metallic rutile IrO_2

X. Xu,[1,*] J. Jiang,[2,3,4,*] W. J. Shi,[5] Vicky Süß,[5] C. Shekhar,[5] S. C. Sun,[1] Y. J. Chen,[1] S.-K. Mo,[4] C. Felser,[5] B. H. Yan,[5] H. F. Yang,[2] Z. K. Liu,[2] Y. Sun,[5] L. X. Yang,[1,6,†] and Y. L. Chen[1,2,3,‡]

[1]*State Key Laboratory of Low Dimensional Quantum Physics, Department of Physics, Tsinghua University, Beijing 100084, People's Republic of China*

[2]*School of Physical Science and Technology, ShanghaiTech University, Shanghai, People's Republic of China*

[3]*Department of Physics, University of Oxford, Oxford, OX1 3PU, United Kingdom*

[4]*Advanced Light Source, Lawrence Berkeley National Laboratory, Berkeley, California 94720, USA*

[5]*Max Planck Institute for Chemical Physics of Solids, D-01187 Dresden, Germany*

[6]*Collaborative Innovation Center of Quantum Matter, Beijing 100084, People's Republic of China*

(Received 10 March 2019; revised manuscript received 17 April 2019; published 3 May 2019)

Using high-resolution angle-resolved photoemission spectroscopy and *ab initio* calculation, we have studied the bulk and surface electronic structure of metallic rutile 5*d* transition metal oxide IrO_2 that harbors both edge and corner sharing Ir-O octahedrons. We observe strong modulation of the band structure by spin-orbit coupling (SOC). The measured band structure is well reproduced by our *ab initio* calculation without band renormalization, suggesting the absence of the SOC-enhanced correlation effect in IrO_2. In accordance with the calculation, we visualize two types of Dirac nodal lines (DNLs) protected by mirror symmetry and nonsymmorphic crystal symmetry, respectively. SOC gaps the first type of DNLs, which may contribute largely to the strong spin Hall effect. The second type of DNLs at the edges of Brillouin zone, however, remain intact against SOC. Our results not only provide important insights into the exotic transport properties of IrO_2, but also shed light on the understanding of the role of SOC in the iridate family.

DOI: 10.1103/PhysRevB.99.195106

I. INTRODUCTION

Iridates represent a particular family of transition metal oxides with rich and fascinating properties such as metal insulator transition [1–3], cuprate-like behaviors [4–6], unusual magnetism [7–9], spin liquid behavior [10,11], and quantum topological phases [12–14]. Behind these intriguing phenomena, strong spin-orbit coupling (SOC) from heavy iridium atoms is believed to play a decisive role. However, it is challenging to unveil the specific role of SOC in the physical properties by experimental techniques without momentum resolution such as transport measurement. Instead, the SOC effect is usually manifested by strong modulation of the electronic structure. A prime example is the band narrowing by the exotic $J_{\text{eff}} = 1/2$ ground state in Sr_2IrO_4 due to the SOC-enhanced electron correlation, which leads to an exotic Mott insulator state [4,6]. In order to further understand the role of SOC in the physics of iridates, it is highly important to investigate the modification of their electronic structures by strong SOC.

Among the family of iridates, the rutile oxide IrO_2 has attracted great research attention. It has the simplest binary chemical composition without extra metal cations in the iridate system, which provides an ideal platform to explore the intrinsic SOC effect from Ir atoms. Although the role of strong SOC in IrO_2 has been widely proven by various experimental results, such as optical spectroscopy [15], x-ray absorption spectroscopy [16], angle-resolved photoemission spectroscopy (ARPES) [17–19] and resonant x-ray diffraction experiment [20], there is still heavy debate regarding the existence of the SOC-enhanced $J_{\text{eff}} = 1/2$ state in the metallic IrO_2 [16,20–22]. Interestingly, IrO_2 exhibits a strong spin Hall effect [23], which is still barely understood. Theoretical calculation has predicted the existence of multiple Dirac nodal lines (DNLs) in IrO_2 and suggested their close connection with the observed spin Hall effect [24], which proposes further experimental and theoretical investigation of its electronic structure. Moreover, IrO_2 promises broad application potentials such as spin valves and spin detectors in spintronics [23], oxygen barriers, and electrodes in memory devices [25], and stable water splitting catalyst in electrochemical [26]. It is thus of great interest and importance to investigate the three-dimensional (3D) electronic structure of IrO_2 in order to further understand the role of SOC and predicted DNLs in its physical properties.

Based on the above motivation, in this work, we comprehensively investigate the 3D electronic structure of IrO_2 using high-resolution ARPES and *ab initio* calculations. The energy bands over the 3D Brillouin zone (BZ) show very weak electronic correlation, although the SOC induces clear energy gaps in the band structure, suggesting the absence of SOC-enhanced electron correlation in IrO_2. Moreover, we identify two types of DNLs and surface states that may be crucial

*These authors contributed equally to this work.
†lxyang@tsinghua.edu.cn
‡yulin.chen@physics.ox.ac.uk

for the transport properties of IrO_2. Our results will not only help understand the exotic electronic properties of IrO_2, but also shed light on the comprehension of the interplay between electronic correlation, strong SOC, and lattice structure in 5*d* transition metal oxides.

II. EXPERIMENT

High quality IrO_2 single crystals were synthesized by flux method [27]. ARPES measurements were performed at the beamline 4.0.3 and beamline 10.0.1 of the Advance Light Source (ALS), and beamline I05 of the Diamond Light Source (DLS) with an overall energy resolution better than 20 meV and a base pressure better than 1.5×10^{-10} Torr. Density functional theory calculations were performed using the Vienna *ab initio* Simulation Package (VASP) [28] with a plane-wave basis. The interactions between the valence electrons and ion cores were described using the projector augmented wave method. The exchange and correlation energy were formulated using the generalized gradient approximation with the Perdew-Burke-Ernzerhof scheme. The plane-wave basis cut off energy was set to 500 eV. Γ-centered k points with a spacing of $0.03\,\text{Å}^{-1}$ were used for the first BZ sampling. The local density of states is relative to the image part of the semi-infinite surface Green's function based on the tight-binding Hamiltonian. The tight-binding Hamiltonian was constructed by projecting the Bloch states into the atomic orbital like Wannier function supplied by the Wannier 90 code.

III. RESULTS AND DISCUSSION

IrO_2 single crystal crystallizes into the rutile-type structure with lattice constants $a = b = 4.498$ Å and $c = 3.154$ Å (space group $P4_2/mnm$, No. 136), as shown in Figs. 1(a) and 1(b) [27]. It shares the common IrO_6 octahedrons as the basic structure component, similar to other iridium oxides. The IrO_6 octahedrons stack in a body-centered structure, forming both corner and edge sharing networks. It can be naturally cleaved along the (110) direction, inducing a clean sample surface for ARPES measurements (see the Supplemental Material [29]). Figure 1(c) shows core-level photoemission spectrum of IrO_2 with clear Ir 4*f* and 5*p* peaks. Intensity of the valence bands in Fig. 1(c) is magnified by a factor of ten to reveal the diversity of Ir 5*d* components near the Fermi level, which is key to most of its physical properties as well as chemical applications such as stable high-efficiency catalyst for water splitting [30].

According to our *ab initio* calculations, IrO_2 harbors two types of DNLs without SOC as indicated by blue and green curves in Fig. 1(d). It should be noted that crystalline symmetries, shown in Figs. 1(a) and 1(b), play an important role in forming DNLs. The first type of DNLs originate from the anticrossing of d_{x2-y2} and $d_{xz,yz}$ bands and is protected by mirror symmetry along the (110) and (10) planes marked by $m(110)$ and $m(\bar{1}10)$ in Fig. 1(b). They disperse within (110) and (10) mirror planes in BZ and form hextuple points (HP) and octuplet points (OP) along the Γ*Z* and *AM* directions, respectively, as shown in Fig. 1(e). The second type of DNLs is promised by the nonsymmorphic symmetry including a fourfold screw rotation around the z axis $\tilde{C}_{4z}$ and a glide

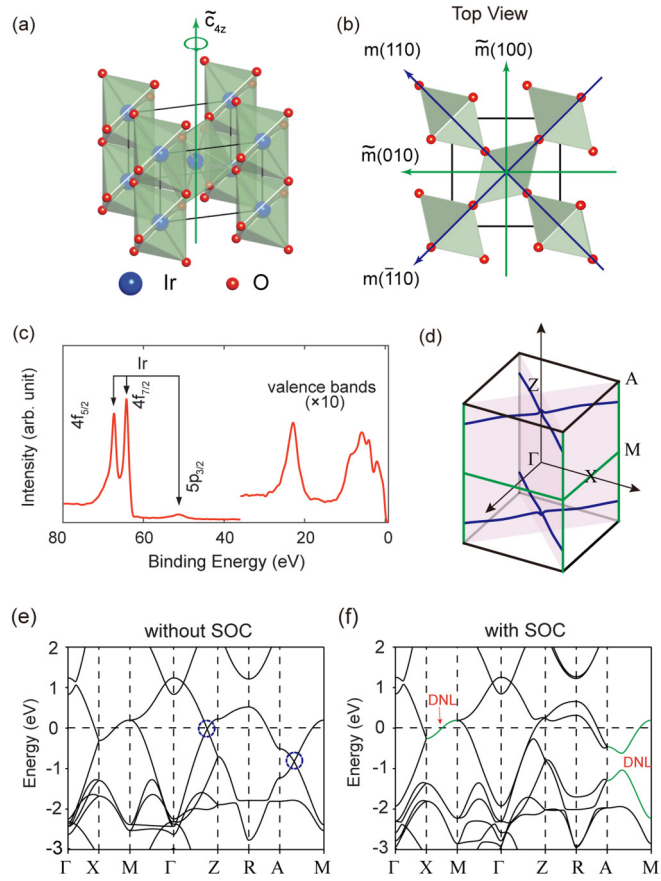

FIG. 1. Overview of the crystalline symmetry of IrO2 and band structure (a) Bird-eye view and (b) Top view of crystal structure of IrO_2. Critical symmetry operations are indicated upon the lattice. (c) Core-level photoemission spectrum clearly showing iridium 4*f* and 5*p* peaks. (d) Theoretically predicted DNLs in three-dimensional (3D) Brillouin zone (BZ) of IrO_2 [first type of Dirac nodal lines (DNLs) in blue, while second type of DNLs appear in green]. The light purple planes indicate the mirror planes. (e), (f) Calculated bulk electronic structure of IrO_2 (e) without and (f) with spin-orbit coupling. Blue dotted circles and green lines indicate the position of DNLs.

mirror reflection along the (100) and (010) planes [$\tilde{m}(100)$ and $\tilde{m}(010)$]. Strong SOC gaps the first type of DNLs, while the second type of DNLs survive along the *AM* and *MX* directions [24]. Figures 1(e) and 1(f) show the calculated band dispersions along high symmetry directions with and without SOC, respectively. SOC lifts the band degeneracy and induces energy gaps at the HP and OP, which are ideal indicators for the modulation of the electronic structure by SOC.

The corresponding 3D BZ and its projected (110) surface BZ are presented in Fig. 2(a) with high symmetry points indicated. According to our theoretical calculation, the Fermi surface (FS) consists of a crossed concentric-reducer-like structure (FS1) along the *ZR* direction [brown pockets in Fig. 2(b)] and a nearly flat structure (FS2) parallel to the *RAMX* plane [cyan pockets in Fig. 2(b)], as well as an ellipsoid (FS3) near the *M* point [green pockets in Fig. 2(b)]. Notably, both FS1 and FS2 are open FSs, which may play important roles in transport properties of IrO_2 under high magnetic field [31]. Figures 2(c)–2(e) show the calculated bulk FS's

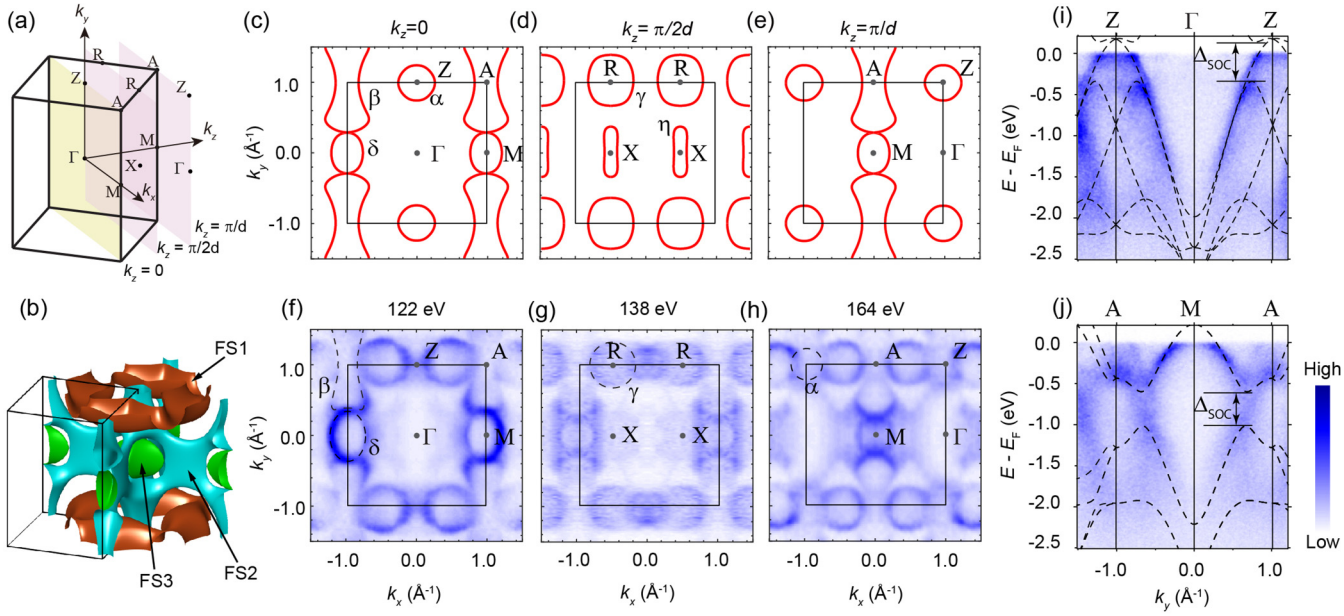

FIG. 2. Three-dimensional electronic structure of IrO_2 (a) Illustration of the 3D BZ of IrO_2, with the indication of planes at $k_z = 0$, $k_z = \pi/2d$, and $k_z = \pi/d$. (b) Calculated Fermi surface structure of IrO_2. (c)–(e) Calculated bulk FS at $k_z = 0$ (f), $k_z = \pi/2d$ (g) and $k_z = \pi/d$ (h). (f)–(h) Photoemission intensity map in the k_x-k_y plane obtained at different photon energies. (i), (j) Measured band dispersion along ZΓZ (i) and AMA (j) directions. The calculated bulk band structure (dashed lines) are overlaid for comparison. Data were collected at 10 K.

at different k_z's. In the ΓZAM plane ($k_z = 0$), there exist a circular pocket α centered at Z, an elliptical pocket δ centered at M and a "dog-bone" like pocket β at A. The β and δ pockets are degenerate along AM due to the DNL protected by the nonsymmorphic crystal symmetry. The FSs show strong k_z variation. In the $XRRX$ plane [Fig. 2(d)], we observe a large elliptical pocket γ at R and a racetrack-like pocket η at X. Since the sample is cleaved along (110) direction, the FS's at $k_z = 0$ and $k_z = \pi/d$ [$d = \sqrt{2}a/2$ is the interlayer distance along (110) direction] have the same structure. In order to experimentally visualize the 3D bulk FS, we conduct photon energy dependent ARPES experiment. The FSs measured at 122, 138, and 164 eV are presented in Figs. 2(f)–2(h), which correspond to $k_z = 0$, $\pi/2d$ and π/d, respectively (see the Supplemental Material [29]). Due to the limited k_z resolution and the strong k_z dispersion of the bulk bands, the measured FS is strongly complicated by the projected features from different k_z's. Nevertheless, we can still distinguish the FS sheets, such as the α, β, δ, and γ pockets. Our experiment and calculation show overall agreement, including the Fermi pocket positions and sizes.

Figures 2(i) and 2(j) show band dispersions along high symmetry directions. For a direct comparison, we superimpose the calculated bulk bands on top of the experiments without renormalization. We observe a good agreement between experiment and calculation in a large energy range, suggesting very weak correlation effect in IrO_2. In consistence with the calculation, the first type of DNLs that are protected by mirror symmetry are indeed gapped by strong SOC effect and the predicted energy gaps induced by SOC are directly observed along both ΓZ and AM as indicated in Figs. 2(i) and 2(j). It is proposed that the SOC-gapped DNLs play decisive roles in the strong spin Hall effect in IrO_2, the mechanism of which calls for further investigation [23]. The gap at HP introduces a unique electronic structure with an energy band dispersing through the gap and connecting the upper and lower part of the gapped band [Fig. 2(i)], in good agreement with calculation. The observed weak correlation effect and strong SOC effect suggest the absence of the SOC-enhanced correlation effect in IrO_2.

In order to further unveil the fine electronic structure of IrO_2, we conduct ARPES measurements using lower photon energy with enhanced energy resolution in Fig. 3. Due to the surface sensitivity of low energy photons, the ARPES spectra are dominated by the photoelectrons from the surface. Thus we use the surface BZ (black rectangles in Fig. 3) to illustrate the in-plane electronic structures. The band structure measured with photons at 80 eV (near $k_z = \pi/d$) is presented in a 3D plot in Fig. 3(a). The high quality of our data enables us to resolve the details of the electronic structure. We reveal an arc-like structure δ centered at $\bar{\Gamma}$, a "dog-bone" like electron pocket β at $\bar{Y}$ and a hole pocket γ at $\bar{M}$ from the constant energy contours at E_F and 150 meV as shown in Figs. 3(b) and 3(d), which are well reproduced by the surface projected band calculations in Figs. 3(c) and 3(e). The band dispersions along different cuts are plotted in Figs. 3(f) and 3(g). The side-by-side comparison between experiment and calculation again shows good agreement, consistent with the weak correlation effect in IrO_2. In addition to the bulk states, the enhanced surface sensitivity enables us to observe the surface states [marked as SS_1 and SS_2 in Figs. 3(b) and 3(c)], which are well captured by our calculations. SS_2 disperses strongly along the edge sharing IrO_6 chains, while SS_1 shows shallow dispersions along both $\bar{\Gamma}\bar{Y}$ and $\bar{\Gamma}\bar{X}$. The origin of these surface states and their possible roles in the transport properties of IrO_2 deserve further studies.

According to *ab initio* calculations, there exist DNLs protected by the nonsymmorphic crystal structure of IrO_2 even

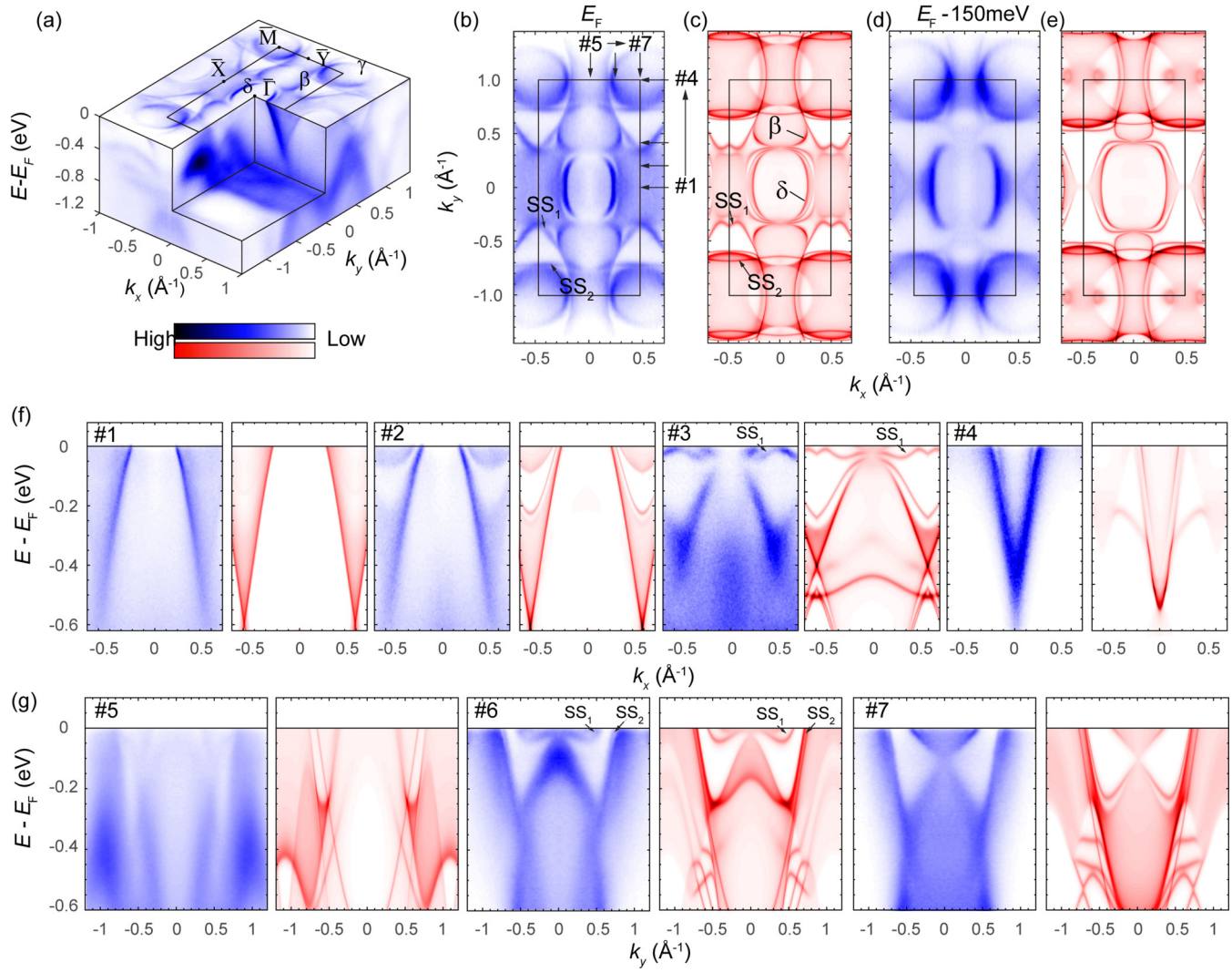

FIG. 3. Details of the electronic structure of IrO_2 (a) 3D plot of the band structure of IrO_2 measured with 80 eV photons. (b)–(e) Comparison between experimental (b, d) and calculated (c, e) constant energy contours at different binding energies. (f), (g) Comparison between experimental and calculated band dispersions along different cuts that are parallel to k_x and k_y, as indicated in panel (b). The experimental and calculated data are shown in blue and red false-color plots, respectively. Data were symmetrized along $\bar{\Gamma}\bar{X}$ and $\bar{\Gamma}\bar{Y}$ for a better comparison with calculation.

under strong SOC, as shown in Fig. 1(c) and schematically illustrated in Figs. 4(a) and 4(d). In order to visualize the DNLs, we show the dispersions along *MA* and *XM* using 164 and 80 eV, respectively, in Figs. 4(b) and 4(e). We directly observe the dispersion of the DNL along *MA* [Fig. 4(b)]. The dispersions perpendicular to the DNL along *MA* are shown in Fig. 4(c), which clearly show the evolution of the Dirac points along the DNL. In addition to the DNL along *MA*, we also observe the projection of the nodal line along *MX* on the Γ*MZ* plane. Figure 4(d) schematically shows the calculated nodal line along *MX* direction. We observe the projection of this nodal line into the Γ*MZ* plane as shown in Fig. 4(e). Figure 4(f) shows the evolution of the dispersions perpendicular to the nodal line, which verifies the existence of Dirac points. Detailed analysis of the second type of DNLs is also shown in the Supplemental Material [29]. Up to now, DNLs protected by nonsymmorphic symmetry have been widely observed in different systems [32]. However, the DNLs usually reside far away from E_F. For example, similar DNLs have been observed by ARPES in ZrSiS [33,34] and InBi [35], which are hundreds of meV away from the Fermi level. In contrast, the DNLs in IrO_2 cross the Fermi level, which provides an ideal platform to realize a possible application of DNLs.

Recently, two analogous types of DNLs have been experimentally observed in RuO_2 that is isostructural with IrO_2 [36]. Two points should be noted concerning the similarities and differences of the DNL properties in RuO_2 and IrO_2: (i) Despite the overall similarity of band structures, the chemical potential in IrO_2 is relatively higher than that in RuO_2 by about 600 meV due to the different electron filling level [24,37]. Thus, the energy of the first type of DNL, which is slightly gapped by SOC, is much higher than the Fermi level, leading to a minor influence upon the exotic transport properties such as spin Hall effect in RuO_2. By contrast, both types of DNLs in IrO_2 directly cross the Fermi level, which

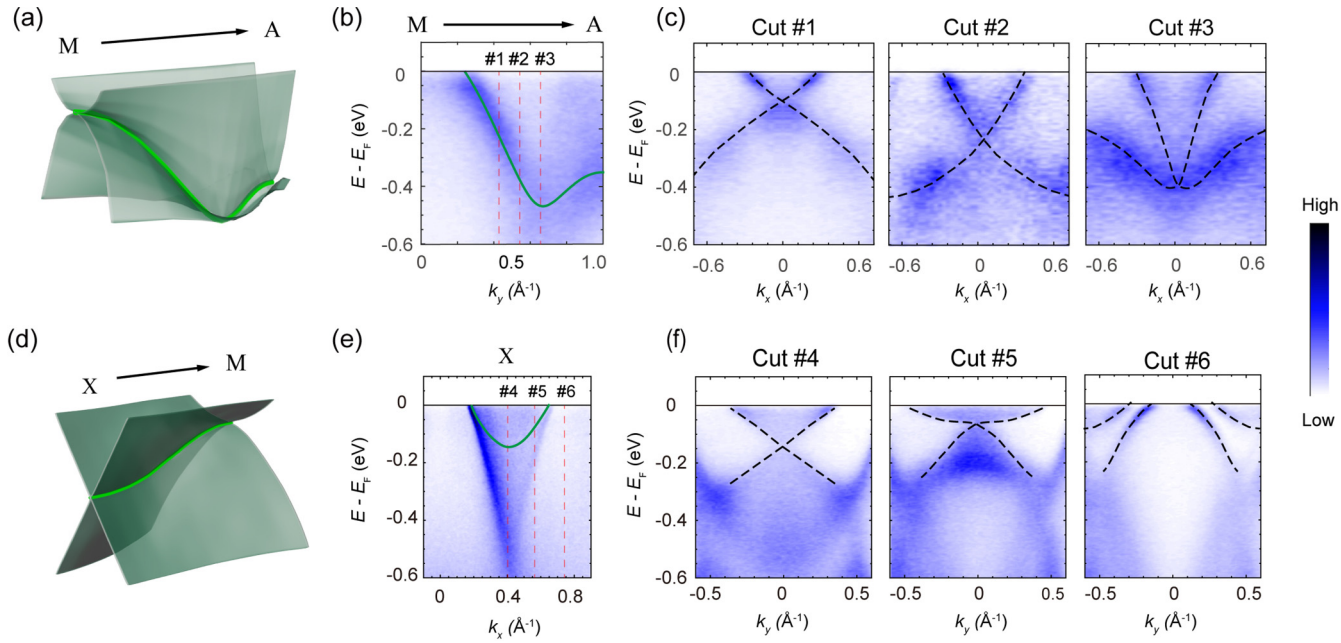

FIG. 4. The second type of DNLs protected by nonsymmorphic crystal symmetries. (a) 3D illustration of the calculated Dirac nodal line along the *MA* direction in IrO_2. (b) Band dispersion along the *MA* direction. The green curve indicates the calculated nodal line. (c) Band dispersions along different momentum cuts perpendicular to the *MA* direction, as indicated in panel (b). (d) 3D illustration of the calculated Dirac nodal line along the *MX* direction. (e) Band dispersion along MX. The green curve indicates the calculated nodal line. (f) Band dispersions along different momentum cuts perpendicular to the *MX* direction, as indicated in panel (e).

not only results in the strong spin Hall effect [23], but may also contribute to other transport phenomena such as the 3D quantum Hall effect [38]. (ii) In comparison with IrO_2, the SOC is relatively weak and negligible in RuO_2, giving rise to the observation of an additional type of DNL (DNL3) in RuO_2 [36]. Indeed, in the absence of SOC, the nonsymmorphic symmetry guarantees band degeneracies in the whole *XMAR* plane including the *XR* direction hosting DNL3 in RuO_2. When the SOC is included, however, DNLs only survive along the edges of the BZ. Therefore, DNL3 is largely gapped in IrO_2, as revealed by both our calculation and photoemission results, which further emphasizes the importance of SOC in IrO_2.

IV. SUMMARY

To summarize, we have presented a comprehensive understanding of the 3D electronic structure of the rutile oxide IrO_2. We observe strong modulation of the band structure by SOC, while the correlation effect is very weak suggesting a negligible impact of the SOC-enhanced correlation effect in metallic IrO_2. We directly visualize the DNLs that are protected by nonsymmorphic crystal symmetry and identify surface states, which may be important to the intriguing transport properties of IrO_2. Our results provide important insights into the modulation of the band structure of iridium oxides by the SOC and crystal symmetry, which will shed light on the understanding of their exotic properties.

ACKNOWLEGMENTS

This paper was supported by the National Natural Science Foundation of China (Grants No. 11774190, No. 11674229, and No. 11634009), the National Key R&D program of China (Grants No. 2017YFA0304600, No. 2017YFA0305400, and No. 2017YFA0402900), the EPSRC (UK) Platform Grant (Grant No. EP/M020517/1). This research used resources of the Advanced Light Source, which is a Department of Energy (DOE) Office of Science User Facility under Contract No. DE-AC02-05CH11231.

[1] H. Zhang, K. Haule, and D. Vanderbilt, Phys. Rev. Lett. **118**, 026404 (2017).

[2] Z. Tian, Y. Kohama, T. Tomita, H. Ishizuka, T. H. Hsieh, J. J. Ishikawa, K. Kindo, L. Balents, and S. Nakatsuji, Nat. Phys. **12**, 134 (2015).

[3] S. H. Chun, B. Yuan, D. Casa, J. Kim, C.-Y. Kim, Z. Tian, Y. Qiu, S. Nakatsuji, and Y.-J. Kim, Phys. Rev. Lett. **120**, 177203 (2018).

[4] B. J. Kim, H. Ohsumi, T. Komesu, S. Sakai, T. Morita, H. Takagi, and T. Arima, Science **323**, 1329 (2009).

[5] Y. K. Kim, O. Krupin, J. D. Denlinger, A. Bostwick, E. Rotenberg, Q. Zhao, J. F. Mitchell, J. W. Allen, and B. J. Kim, Science **345**, 187 (2014).

[6] B. J. Kim, H. Jin, S. J. Moon, J. Y. Kim, B. G. Park, C. S. Leem, J. Yu, T. W. Noh, C. Kim, S. J. Oh, J. H. Park, V. Durairaj, G. Cao, and E. Rotenberg, Phys. Rev. Lett. **101**, 076402 (2008).

[7] J. Chaloupka, G. Jackeli, and G. Khaliullin, Phys. Rev. Lett. **105**, 027204 (2010).

[8] G. Jackeli and G. Khaliullin, Phys. Rev. Lett. **102**, 017205 (2009).

[9] M. A. Laguna-Marco, D. Haskel, N. Souza-Neto, J. C. Lang, V. V. Krishnamurthy, S. Chikara, G. Cao, and M. van Veenendaal, Phys. Rev. Lett. **105**, 216407 (2010).

[10] T. Dey, A. V. Mahajan, P. Khuntia, M. Baenitz, and B. Koteswararao, F. C. Chou, Phys. Rev. B **86**, 140405(R) (2012).

[11] M. J. Lawler, A. Paramekanti, Y. B. Kim, and L. Balents, Phys. Rev. Lett. **101**, 197202 (2008).

[12] M. C. Shapiro, S. C. Riggs, M. B. Stone, C. R. de la Cruz, S. Chi, A. A. Podlesnyak, and I. R. Fisher, Phys. Rev. B **85**, 214434 (2012).

[13] X. Wan, A. M. Turner, A. Vishwanath, and S. Y. Savrasov, Phys. Rev. B **83**, 205101 (2011).

[14] A. Shitade, H. Katsura, J. Kuneš, X.-L. Qi, S.-C. Zhang, and N. Nagaosa, Phys. Rev. Lett. **102**, 256403 (2009).

[15] J. S. de Almeida and R. Ahuja, Phys. Rev. B **73**, 165102 (2006).

[16] J. P. Clancy, N. Chen, C. Y. Kim, W. F. Chen, K. W. Plumb, B. C. Jeon, T. W. Noh, and Y.-J. Kim, Phys. Rev. B **86**, 195131 (2012).

[17] J. K. Kawasaki, M. Uchida, H. Paik, D. G. Schlom, and K. M. Shen, Phys. Rev. B **94**, 121104(R) (2016).

[18] P. K. Das, J. Sławińska, I. Vobornik, J. Fujii, A. Regoutz, J. M. Kahk, D. O. Scanlon, B. J. Morgan, C. McGuinness, E. Plekhanov, D. Di Sante, Y.-S. Huang, R.-S. Chen, G. Rossi, S. Picozzi, W. R. Branford, G. Panaccione, and D. J. Payne, Phys. Rev. Mater. **2**, 065001 (2018).

[19] J. K. Kawasaki, C. H. Kim, J. N. Nelson, S. Crisp, C. J. Zollner, E. Biegenwald, J. T. Heron, C. J. Fennie, D. G. Schlom, and K. M. Shen, Phys. Rev. Lett. **121**, 176802 (2018).

[20] Y. Hirata, K. Ohgushi, J.-i. Yamaura, H. Ohsumi, S. Takeshita, M. Takata, and T.-H. Arima, Phys. Rev. B **87**, 161111(R) (2013).

[21] S. K. Panda, S. Bhowal, A. Delin, O. Eriksson, and I. Dasgupta, Phys. Rev. B **89**, 155102 (2014).

[22] W. J. Kim, S. Y. Kim, C. H. Kim, C. H. Sohn, O. B. Korneta, S. C. Chae, and T. W. Noh, Phys. Rev. B **93**, 045104 (2016).

[23] K. Fujiwara, Y. Fukuma, J. Matsuno, H. Idzuchi, Y. Niimi, Y. Otani, and H. Takagi, Nat. Commun. **4**, 2893 (2013).

[24] Y. Sun, Y. Zhang, C.-X. Liu, C. Felser, and B. Yan, Phys. Rev. B **95**, 235104 (2017).

[25] Y. J. Song, H. H. Kim, S. Y. Lee, D. J. Jung, B. J. Koo, J. K. Lee, Y. S. Park, H. J. Cho, S. O. Park, and K. Kim, Appl. Phys. Lett. **76**, 451 (2000).

[26] C. C. L. McCrory, S. Jung, J. C. Peters, and T. F. Jaramillo, J. Am. Chem. Soc. **135**, 16977 (2013).

[27] S. R. Butler and J. L. Gillson, Mater. Res. Bull. **6**, 81 (1971).

[28] G. Kresse and J. Furthmüller, Phys. Rev. B **54**, 11169 (1996).

[29] See Supplemental Material at http://link.aps.org/supplemental/10.1103/PhysRevB.99.195106 for (I) Sample characterization, (II) kz dispersion of IrO2, and (III) detailed analysis of the second type of Dirac nodal lines.

[30] Y. Ping, G. Galli, and W. A. Goddard, The J. Phys. Chem. C **119**, 11570 (2015).

[31] J. J. Lin, S. M. Huang, Y. H. Lin, T. C. Lee, H. Liu, X. X. Zhang, R. S. Chen, and Y. S. Huang, J. Phys.: Condens. Matter **16**, 8035 (2004).

[32] S.-Y. Yang, H. Yang, E. Derunova, S. S. P. Parkin, B. Yan, and M. N. Ali, Adv. Phys. X **3**, 1414631 (2018).

[33] C. Chen, X. Xu, J. Jiang, S. C. Wu, Y. P. Qi, L. X. Yang, M. X. Wang, Y. Sun, N. B. M. Schröter, H. F. Yang, L. M. Schoop, Y. Y. Lv, J. Zhou, Y. B. Chen, S. H. Yao, M. H. Lu, Y. F. Chen, C. Felser, B. H. Yan, Z. K. Liu, and Y. L. Chen, Phys. Rev. B **95**, 125126 (2017).

[34] L. M. Schoop, M. N. Ali, C. Straßer, A. Topp, A. Varykhalov, D. Marchenko, V. Duppel, S. S. P. Parkin, B. V. Lotsch, and C. R. Ast, Nat. Commun. **7**, 11696 (2016).

[35] S. A. Ekahana, S.-C. Wu, J. Jiang, K. Okawa, D. Prabhakaran, C.-C. Hwang, S.-K. Mo, T. Sasagawa, C. Felser, B. Yan, Z. Liu, and Y. Chen, New J. Phys. **19**, 065007 (2017).

[36] V. Jovic, R. J. Koch, S. K. Panda, H. Berger, P. Bugnon, A. Magrez, K. E. Smith, S. Biermann, C. Jozwiak, A. Bostwick, E. Rotenberg, and S. Moser, Phys. Rev. B **98**, 241101(R) (2018).

[37] L. F. Mattheiss, Phys. Rev. B **13**, 2433 (1976).

[38] J.-W. Rhim and Y. B. Kim, Phys. Rev. B **92**, 045126 (2015).